J Appl Electrochem (2013) 43:1131–1144
DOI 10.1007/s10800-013-0566-x

ORIGINAL PAPER

Reduction of CO_2 to CO at Cu–ceria-gadolinia (CGO) cathode in solid oxide electrolyser

C-Y. Cheng · G. H. Kelsall · L. Kleiminger

Received: 31 January 2013 / Accepted: 14 May 2013 / Published online: 30 May 2013

Abstract The feasibility was investigated of using a Cu/CGO cathode for CO_2 reduction to CO in a high temperature solid oxide electrolyser (CO_2–CO, Cu/CGO|YSZ|YSZ/LSM|LSM, ambient air). An adherent layer of porous Cu/CGO electrode on YSZ electrolyte was achieved by sintering Cu/CGO paste at 1,000 °C for 5 h. Comparable performance was obtained with Ni/YSZ and Cu/CGO cathodes for CO_2 reduction at 750 °C and a 50:50 CO_2–CO feed; CO oxidation rates were faster than CO_2 reduction rates. Ohmic and polarisation resistances of the Cu/CGO electrode all decreased with decreasing CO_2:CO feed ratio. In the electrolytic mode, 100 % current efficiency for CO_2 reduction to CO was achieved on the Cu/CGO cathode at potential differences up to 1.5 V, above which the electronic conductivity of the YSZ electrolyte increased, causing a loss in effective current efficiency. Further increase in potential difference to ca. >2.3 V caused irreversible damage to the YSZ electrolyte due to its partial decomposition. No significant performance degradation, Cu sintering/migration, carbon deposition or electrode delamination was evident during 2 h of operating the electrolyser at 1.85 V and 750 °C for CO_2 reduction with a Cu/CGO cathode.

Keywords Carbon dioxide reduction · Solid oxide electrolyser · Copper cathode · Ceria-gadolinia · Yttria-stabilised zirconia (YSZ)

List of symbols

$E(T)$	Equilibrium potential at temperature T taking into account the reactants' and products' composition (V)
E	Potential difference corrected for ohmic drop, calculated by Eq. (6) (V)
E_{app}	Applied potential of the fuel electrode with respect to LSM ring reference electrode exposed to air (V)
E_{dp}	Decomposition potential of electrolyte (V)
$\Delta E^{\theta}_{CO_2/CO,T}$	Equilibrium potential for the electrolysis of CO_2, reaction (17) (V)
$\Delta E^{\theta}_{ZrO_2/Zr,T}$	Equilibrium potential for the decomposition of ZrO_2, reaction by reaction (10) (V)
$\Delta E^{\theta}_{CeO_2/Ce_2O_3,T}$	Equilibrium potential for the reduction of CeO_2 to Ce_2O_3, reaction (12) (V)
F	Faraday constant, 96 485 (C mol^{-1})
$\Delta_r G^{\theta}_T$	Change in Gibbs free energy at temperature T (J mol^{-1})
I	Current (A)
j	Current density (A cm^{-2})
k	Boltzmann's constant, 8.614×10^{-5} (eV K^{-1})
dn/dt	Change in amount of CO_2 or CO with time (mol s^{-1})
O_O	Oxygen at a regular oxygen site
$V_{\ddot{O}}$	A vacant positively charged oxygen site
P_{O_2}	Oxygen partial pressure (atm)
P_{CO_2}	Carbon dioxide partial pressure (atm)
P_{CO}	Carbon monoxide partial pressure (atm)
R_s	Ohmic resistance (Ω cm^2)
R_p	Polarisation resistance (Ω cm^2)
T	Temperature (K)
σ_{ion}	Ionic conductivity (S cm^{-1})
σ_e	Electronic conductivity (S cm^{-1})
CGO	Cerium-gadolinium oxide, $Gd_{0.10}Ce_{0.90}O_2$

C-Y. Cheng · G. H. Kelsall (✉) · L. Kleiminger
Department of Chemical Engineering, Imperial College London, London SW7 2AZ, UK
e-mail: g.kelsall@imperial.ac.uk

YSZ	Yttria-stabilised zirconia, $(Y_2O_3)_{0.08}(ZrO_2)_{0.92}$
LSM	Lanthanum strontium manganite, $(La_{0.80}Sr_{0.20})MnO_{3-x}$

1 Introduction

Fossil fuels presently constitute our primary energy resource, but there are significant concerns with their security of supply, depletion, costs and the environmental impact of their combustion, producing carbon dioxide and other greenhouse gases that contribute to climate change. An alternative is to use CO_2 as a feed stock, together with renewable energy sources, for fuel production. We report below results of the electrochemical reduction of CO_2 to CO using a solid oxide electrolyser (SOE).

Operating at 500–1,000 °C confers thermodynamic and kinetic benefits on SOEs, decreasing their electrical energy demand [1] by thermal energy input, which also decreases charge transfer and transport overpotentials for cathodic reduction of CO_2 to CO and O^{2-} anions by reaction (1). O^{2-} anions are transported across an oxide ion-conducting electrolyte, such as yttria-stabilised zirconia (YSZ), reaction (2), and evolve as pure O_2 at, e.g. a lanthanum strontium manganite (LSM) anode (air electrode) by reaction (3).

$$\text{Cathode (Fuel electrode):} \quad CO_2 + 2e^- \rightarrow CO + O^{2-} \quad (1)$$

$$\text{YSZ Electrolyte:} \quad O^{2-}_{\text{cathode}} \rightarrow O^{2-}_{\text{anode}} \quad (2)$$

$$\text{Anode (Air electrode):} \quad 0.5O_2 + 2e^- \leftarrow O^{2-} \quad (3)$$

Reduction of CO_2 in SOEs with Pt or Pt/YSZ electrodes and YSZ electrolytes was researched to develop electrochemical processes for O_2 generation for NASA's Mars Missions. The Martian atmosphere contains up to 95.3 % CO_2, which could be reduced in a SOE to produce O_2 for use as life support and propellant oxidant [2–4].

Recent research on CO_2 electrolysis and co-electrolysis of CO_2 and H_2O has been carried out mostly using conventional Ni/YSZ cathodes, used as fuel electrodes in SOFCs. Various groups have reported [1, 5–11] encouraging results of experimental investigations of reactor performance, long-term stability, cause of cell degradation and passivation rate, together with energy and economic analyses for CO_2-neutral renewable liquid fuel energy storage cycles. CO_2/H_2O co-electrolysis in SOEs produced syngas, which was converted to liquid fuel via the Fischer–Tropsch process and subsequently converted back into electricity in a fuel cell, and products from the fuel cell were then recycled back to the electrolyser. The Ni/YSZ fuel electrode exhibited lower overpotentials in the fuel cell mode than in the electrolyser mode; the charge transfer rate for the reduction of CO_2 to CO was slower than that of H_2O to H_2. In co-electrolysis, CO_2 was reduced to CO mainly indirectly by the gas phase reverse water gas shift reaction (WGSR), reaction (4), the cathode reaction being predominately H_2O reduction.

$$H_2 + CO_2 = CO + H_2O \quad (4)$$

It was suggested that a ceria-based electrode was preferable in electrolysis mode, due to its oxygen storage capacity and enhanced cathode activity due to ceria reduction [11]. Ni/cerium-gadolinium oxide (CGO) and Ni/ruthenium (Ru)/CGO fuel electrodes showed better performance than Ni/YSZ; a bi-layer CGO/YSZ electrolyte exhibited significantly better performance than a SOE with either YSZ or CGO electrolyte for CO_2 electrolysis, H_2O electrolysis and co-electrolysis [12].

There are concerns about the stability of Ni/YSZ fuel electrodes in CO_2–CO atmospheres. At high cell voltages and high CO concentrations, Ni catalyses coke formation via the Boudouard disproportionation reaction (5):

$$2CO = CO_2 + C \quad (5)$$

CO disproportionates to form C nanofibres that deposit on the active sites and decrease cell performance. Ni can be reoxidised by pure CO_2 and can damage the Ni/YSZ electrode, so it is important to ensure that the entire Ni/YSZ electrode is under reducing conditions. The efficiency of Ni as a catalyst for CO_2 reduction is also uncertain. As a result, fuel electrodes without Ni, including 40 mol% gadolinia-doped ceria (CGO) [13], p-type perovskite $(La_{0.75}Sr_{0.25})_{0.97}Cr_{0.5}Mn_{0.5}O_{3-\delta}$ (LSCM)/YSZ [14], LSCM/CGO [14, 15], LSCM/YSZ infiltrated with palladium (Pd) and $Ce_{0.48}Zr_{0.48}Y_{0.04}O_2$ (CZY) [16], and n-type perovskite $La_{0.2}Sr_{0.8}TiO_{3+\delta}$ (LST)/CGO [17], have also been investigated for CO_2 electrolysis, H_2O electrolysis and/or co-electrolysis. As for the case with Ni/YSZ and Ni/CGO electrodes, LSCM/CGO electrodes also showed improved performance over LSCM/YSZ electrodes, when the cells were operated in the electrolytic mode [14]. However, the strong reducing potentials required for CO_2 reduction can cause chemical and structural changes to these mixed oxides electrodes; for example, p-type LSCM, with electrons as minority carriers, exhibited large polarisation resistance and LST-based cathodes were partially reduced ($Ti^{4+} \rightarrow Ti^{3+}$) at potentials for CO_2 reduction.

Copper(Cu)-doped $La_{0.58}Sr_{0.4}Co_{0.22}Fe_{0.8}O_{3-\delta}$ (LSCF)/CGO electrodes were tested as cathodes for reducing CO_2 to CO, coupled to hydrogen oxidation in a SOFC for combined power generation with CO_2 reduction [18],

though measured open circuit potential differences were only 0.379 V with 100 % CO_2 feed to the cathode at 800 °C. Cu was added as it has been reported to be an efficient cathode material for electrochemical reduction of CO_2 in aqueous solutions [19]. Gas phase CO_2 reduction activity on Cu-, Ag- and Pt-doped LSCF/CGO cathodes were analysed using temperature-programmed techniques; the effects of dopants on CO_2 reduction kinetics were found to be in the order of Cu > Ag > Pt [20]. Results of using Cu-based fuel electrodes have also been reported for direct oxidation of hydrocarbons in SOFCs to avoid coke formation [21–23]. Due to the lower melting point of CuO (1,599 K) compared to NiO (2,228 K), the sintering temperature of Cu-based electrodes during fabrication was lowered to avoid solid-state reaction. However, lower sintering temperatures could cause problems, in that the electrolyte powders do not sinter properly and Cu diffuses out of the Cu-electrolyte structure during SOFC/SOE operation [24]. The preferred fabrication method was impregnation with aqueous copper nitrate solution of the porous electrolyte matrix, sintering at high temperature previously, followed by sintering at lower temperature to decompose the copper nitrate [23]. More recently, Cu/YSZ cermets were fabricated successfully using high-energy ball milling, followed by sintering at 900 °C; the Cu/YSZ was tested as the fuel electrode in a SOE for H_2O electrolysis at 800 °C [25–27]. Similar performances were achieved with the Cu/YSZ and Ni/YSZ electrodes. Formation of acicular copper crystals on Cu/YSZ occurred after 10 h of operation, but no significant agglomeration of Cu particles was observed. However, there was evidence that even during sintering of the CuO/YSZ electrode at as low as 900 °C in air, CuO reacted with YSZ to produce monoclinic zirconia, possibly by substituting Zr^{4+} with Cu^{2+} in the YSZ lattice, releasing ZrO_2 and destabilising the YSZ [28]. In reducing conditions, the partial reduction of Zr^{4+} to Zr^{3+} was also promoted by Cu.

The performance is reported below of a SOE with a Cu/CGO fuel electrode, YSZ electrolyte and LSM/YSZ air electrode for CO_2 electrolysis. For comparison, the performance of a cell with a Ni/YSZ fuel electrode is also presented. Cu was chosen because it does not catalyse coke formation, it is stable to higher oxygen pressures than Ni, so less likely to reoxidise, and it shows good catalytic activity for CO_2 reduction. CGO was chosen as the ionic conductor in the fuel electrode because it enhances performance in the electrolysis mode and it requires lower sintering temperatures to form a connected network than YSZ. Hence, it is more compatible with the melting point of CuO, so conventional fabrication methods are possible and it helps to minimise reactions between CuO/Cu and YSZ electrolytes during sintering and SOE operation; under oxidising conditions, copper zirconate could be formed.

2 Experimental

2.1 Cell fabrication

Electrolytes used in the cells were 8 mol% yttria-stabilised zirconia, $(Y_2O_3)_{0.08}(ZrO_2)_{0.92}$ (YSZ), as commercial pellets with a diameter of 25 mm and a thickness of 250 μm (NexTech). The lanthanum strontium manganite $(La_{0.80}Sr_{0.20})MnO_{3-x}$ (LSM)/YSZ composite air electrode consisted of two layers: a LSM/YSZ layer and an additional pure LSM layer to improve electrical conductivity. A doctor blade was used to apply LSM/YSZ (50:50 wt%) composite paste (NexTech) to the YSZ electrolyte. After drying on a hot plate at 60 °C for 20 min, pure LSM paste (NexTech) was applied on top of LSM/YSZ layer. After drying on a hot plate for a further 20 min, the two layers were co-sintered in air at 1,100 °C for 3 h at a ramp rate of 4 °C min^{-1}. A pure LSM ring reference electrode with inner and outer diameters of 21 and 19 mm, respectively, was applied with a brush around the air electrode and sintered at the same time as the air electrode.

Cells with two types of fuel electrodes were fabricated. The nickel (Ni)/YSZ fuel electrode was prepared from commercial nickel oxide (NiO)/YSZ (66:34 wt%) paste (NexTech). After drying, it was sintered in air at 1,350 °C for 1 h at ramp rate of 4 °C min^{-1}.

The copper (Cu)/cerium-gadolinium oxide $Gd_{0.10}Ce_{0.90}O_2$ (CGO) cermet fuel electrode was prepared from mixtures of copper oxide (CuO) (Sigma Aldrich) and CGO (NexTech) powders in a weight ratio of 60:40 wt%. Ink vehicle (NexTech) was then added to the resultant powders' mixture to form a paste with solid content of ca. 70 wt%. The paste was applied to the electrolyte by a doctor blade. After drying, it was sintered in air at 1,000 °C for 5 h at a ramp rate of 4 °C min^{-1}.

The sequence of electrode preparation was arranged in the order of descending electrode sintering temperature. Each individual layer had an initial thickness of ca. 80 μm and shrunk to ca. 40 μm after sintering. The fuel and air electrodes had diameters of 11 mm.

Prior to the electrochemical characterisation in CO_2–CO atmospheres, NiO and CuO were fully reduced to Ni and Cu, respectively, in H_2. After reduction, the metal content of both types of fuel electrodes was ca. 50 vol%. Microstructures of the electrodes were imaged using a scanning electron microscope (model TM-1000, Hitachi) after operating in CO_2–CO. The Cu distribution of the Cu/CGO electrode was also mapped using an energy dispersive spectrometer (JSM-6400, JEOL). X-ray diffraction (XRD)

patterns of the CuO and CGO powder, the CuO/CGO electrode after sintering and the Cu/CGO electrode after reduction in H_2 were analysed (X'Pert Pro, PANalytical). The patterns were performed using a Cu X-ray tube ($K\alpha_1 = 1.5406$Å) in the 10°–90° 2θ range with a step size of 0.033° (1 s per step).

2.2 Pellet cell equipment

Pellet cells were attached to an alumina tube (Almath Crucibles) using ceramic cement sealant (Ceramabond 552, Amerco) and placed inside a tube furnace (Elite, model TSU 12/50/120) of 50 mm diameter and 180 mm length. Silver mesh (80 mesh woven from 0.115 mm diameter wire, Alfa Aesar) was used as the current collector for both the anode and cathode. Two silver wires of 0.25 mm diameter (Sigma Aldrich) were spot welded to each silver mesh and two silver wires were attached to the LSM reference ring electrode for external electrical circuit connections. A few drops of conductive silver paste (Alfa Aesar) were applied onto the silver mesh and silver wires to improve electrical contact between the electrodes and the mesh/wire.

Electrochemical measurements were made with an Autolab potentiostat/galvanostat (Metrohm model PGSTAT302N with FRA2 module). The LSM/YSZ air electrode was exposed to ambient air. CO_2, CO, H_2 and He were fed to the fuel electrode with their flow rates controlled by mass flow controllers (Bronkhorst). The outlet gas from the fuel electrode was analysed by a mass spectrometer (Pfeiffer Vacuum Quadstar).

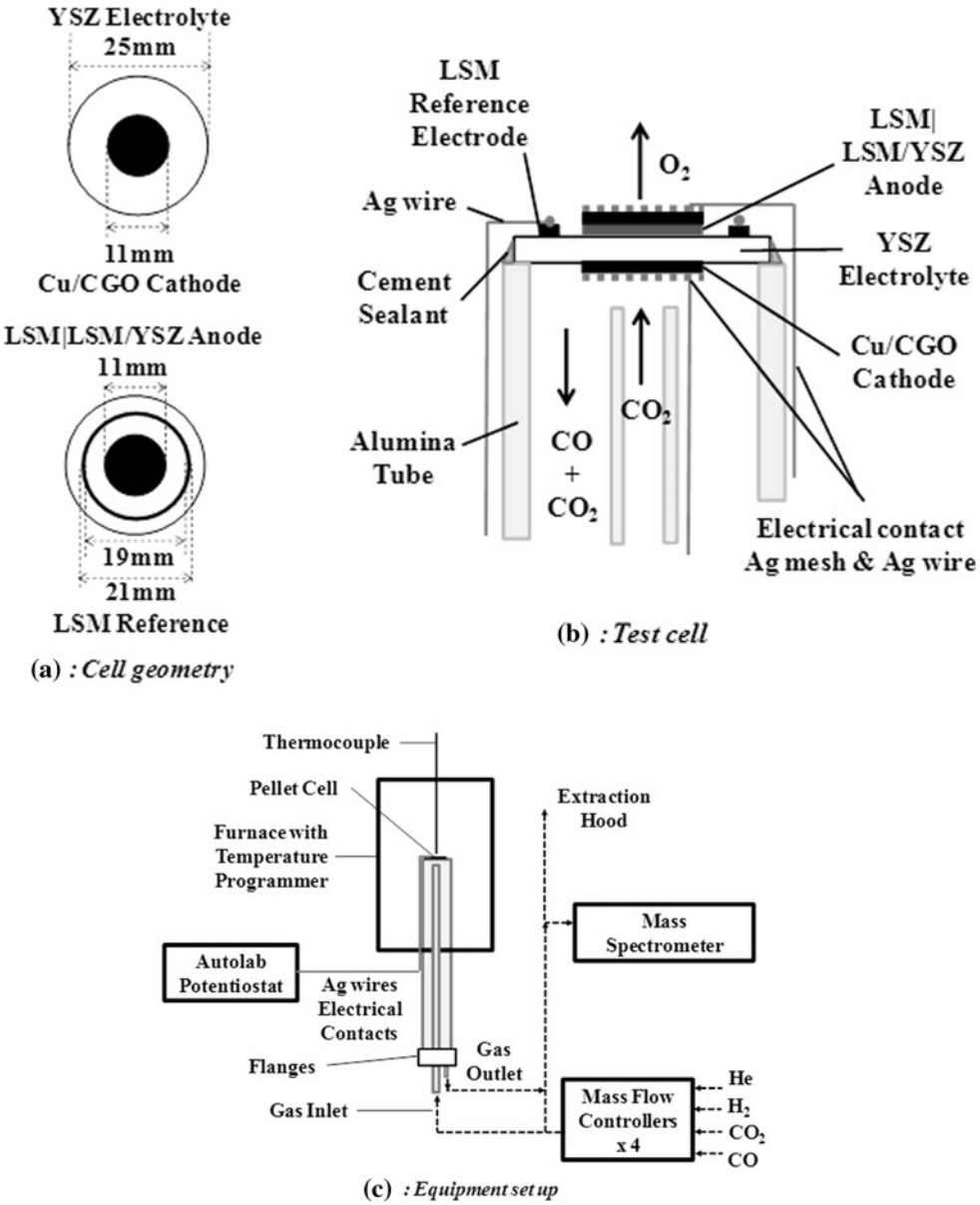

Fig. 1 Schematic diagram of the test rig **a** pellet cell geometry, **b** test cell and **c** equipment and instrumentation

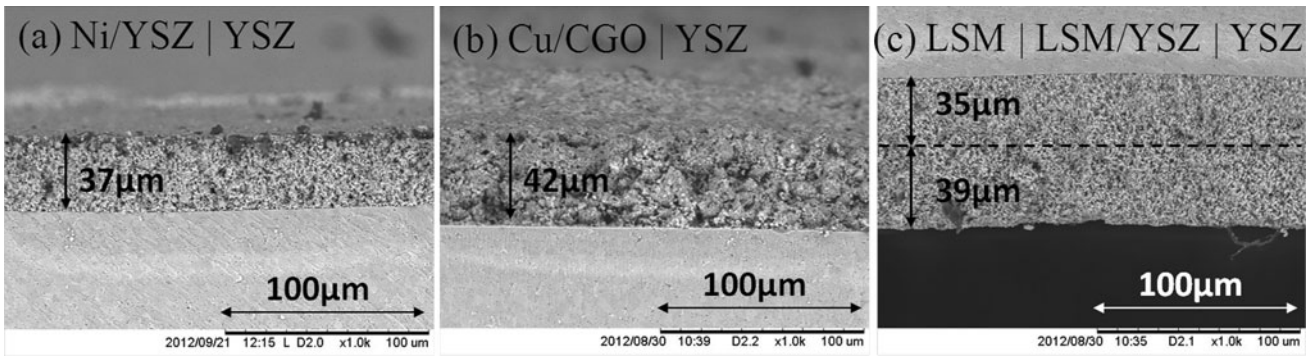

Fig. 2 SEM photomicrographs of cross section of **a** Ni/YSZ|YSZ electrolyte interface, **b** Cu/CGO|YSZ electrolyte interface and **c** LSM|LSM/YSZ|YSZ electrolyte interface, after operating as both SOE and SOFC up to 750°C for 6–8 h

Figure 1 shows schematic diagrams of (a) pellet cell geometry, (b) test cell and (c) equipment and instrumentation.

2.3 Electrochemical characterisation

The pellet cell was heated to 700 °C at a ramp rate of 5 °C min^{-1} in H_2–He (10:90 vol%) at a total flow rate of 50 ml min^{-1}. At 700 °C, the gas was switched to pure H_2. NiO/CuO was reduced to Ni/Cu in pure H_2 for 2 and 0.5 h, respectively. The gas feed to the fuel electrode was then switched to CO_2–CO (50:50 vol%) with a total flow rate of 50 ml min^{-1} and the pellet cell was heated to 750 °C at 5 °C min^{-1}. Open circuit potentials (OCP), impedance spectra, cyclic voltammograms and steady-state potential-current data were obtained, together with CO_2–CO compositions of the outlet gas. All electrochemical measurements were carried out at 750 °C and CO_2–CO (50:50 vol%) feed for both Ni/YSZ and Cu/CGO fuel electrodes unless otherwise stated. For the Cu/CGO fuel electrode, in different CO_2–CO feeds at OCP, impedance spectra were also recorded using a 10 mV p–p perturbation and frequencies from 100 kHz to 0.1 Hz.

3 Results and discussion

3.1 Microstructure of the cells

All SEM images shown are of electrodes after operating as both SOE and SOFC up to 750 °C for 6–8 h. Figure 2 shows the SEM micrographs of a cross-sectional view of (a) Ni/YSZ|YSZ electrolyte interface, (b) Cu/CGO|YSZ electrolyte interface and (c) LSM|LSM/YSZ|YSZ electrolyte interface. Both types of fuel electrodes, Ni/YSZ and Cu/CGO, and the air electrode, LSM|LSM/YSZ, were adherent to the YSZ electrolyte after sintering at 1,350, 1,000 and 1,100 °C, respectively. The thickness of the YSZ electrolyte was 250 µm and the thickness of Ni/YSZ, Cu/CGO, LSM and LSM/YSZ layers was ~40 µm each after sintering. No delamination of electrodes was evident after operating in both SOE and SOFC modes.

Figure 3 shows surfaces of the (a) Ni(50 %)/YSZ, (b) Cu(50 %)/CGO and (c) Cu(85 %)/CGO electrode; the metal content shown is in volume% after reduction from NiO/CuO to Ni/Cu with H_2. The Ni/YSZ electrode, prepared from commercial paste (NexTech), showed a better microstructure than the Cu/CGO electrodes, with smaller particle sizes, more evenly sized and distributed pores and greater density of triple-phase boundaries (TPB). The Cu(50 %)/CGO electrode was porous and the particles connected well together. Due to the high Cu content of the Cu(85 %)/CGO electrode, significant agglomeration of Cu particles occurred, causing much lower porosity and TPB density, leading to poor cell performance, which is not reported here.

Energy dispersive X-ray spectroscopy (EDS) confirmed that the Cu content of the Cu/CGO electrode was 53.5 wt%, corresponding to 48.3 vol%. Figure 4 shows the maps of Cu, cerium (Ce^{IV}) and zirconium (Zr^{IV}) components of the Cu/CGO electrode|YSZ electrolyte interface. Cu and Ce^{IV} were evenly distributed across the Cu/CGO electrode without noticeable Cu migration towards the Cu/CGO|YSZ electrolyte boundary, as observed for a Cu/$Y_{0.2}Ti_{0.18}Zr_{0.62}O_{1.9}$ (YZT) electrode [24].

Figure 5 shows the XRD patterns for (a) the starting material CuO and CGO powder and (b) CuO/CGO electrode after sintering at 1,000 °C and Cu/CGO electrode after reduction in H_2. The peaks for the CuO/CGO electrode matched the corresponding peaks of CuO and CGO powder and there was no indication of formation of other phases. After reduction in H_2, the peaks for CuO diminished and the new peaks matched the peaks for Cu and Cu_2O in the database (X'Pert Pro, PANalytical). The formation of Cu_2O could be due to Cu reoxidised after being taken out of the reactor.

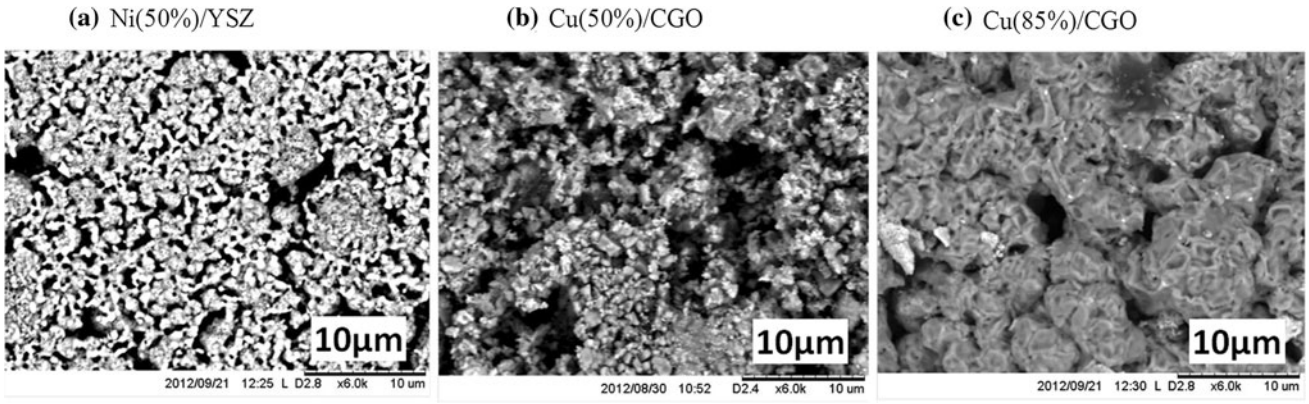

Fig. 3 SEM photomicrographs of surface of **a** Ni(50 %)/YSZ electrode, **b** Cu(50 %)/CGO and **c** Cu(85 %)/CGO electrode, after operating as both SOE and SOFC up to 750°C for 6–8 h

3.2 Performance of the cells

Figure 6 compares the ohmic drop-corrected potential difference (E)–current density (j) relationship of cells with a Ni/YSZ (50 vol% Ni) and a Cu/CGO (50 vol% Cu) electrode, operating in both fuel cell mode (SOFC) and electrolysis mode (SOE) with a feed CO_2–CO ratio of 50:50 at 750 °C. Note that the ohmic drop-corrected potential difference (E) is the applied potential at the fuel electrode (E_{app}) with respect to the reference ring electrode on the opposite side of the YSZ electrolyte, taking into account the ohmic potential drop across the YSZ electrolyte and the fuel electrode, calculated by Eq. (6):

$$E = E_{app} - j \times R_s \quad (6)$$

where j is the current density in A cm^{-2} and R_s is the sum of the ohmic resistance of the YSZ electrolyte and fuel electrode in Ω cm^2, obtained from impedance spectra measured at OCP. Experimental R_s values obtained for Ni/YSZ|YSZ and Cu/CGO|YSZ were 1.23 and 1.73 Ω cm^2, respectively. No significant variation was calculated in R_s for applied potentials between 0.5 and 1.5 V. The ohmic

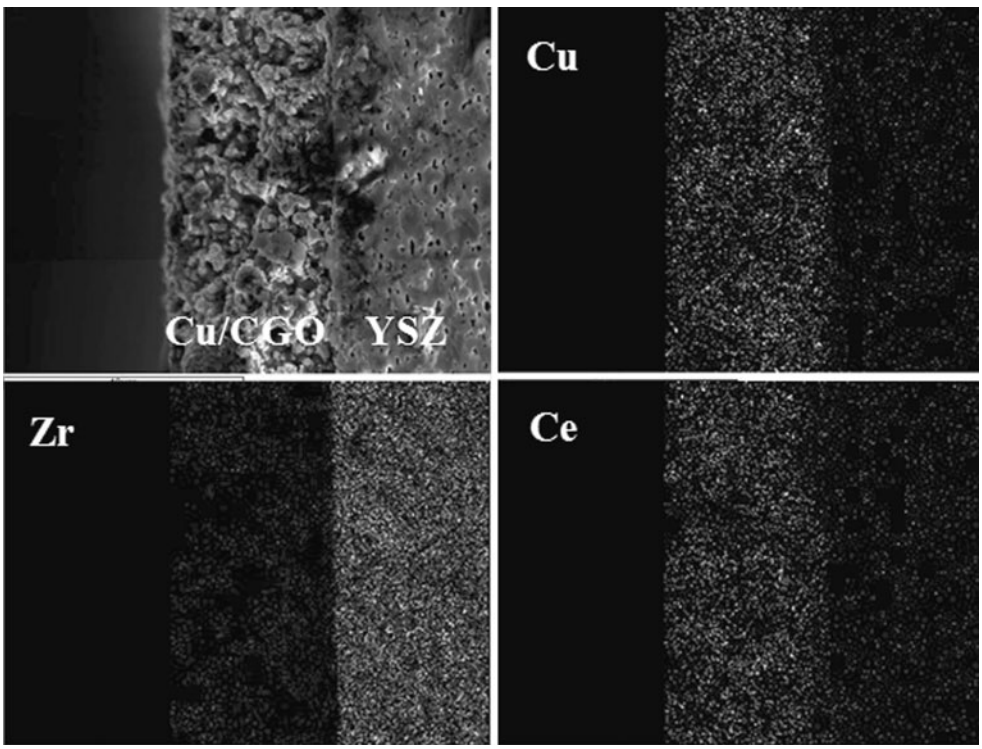

Fig. 4 SEM photomicrograph and EDS mapping of Cu, Ce, Zr components of a Cu/CGO electrode|YSZ electrolyte interface

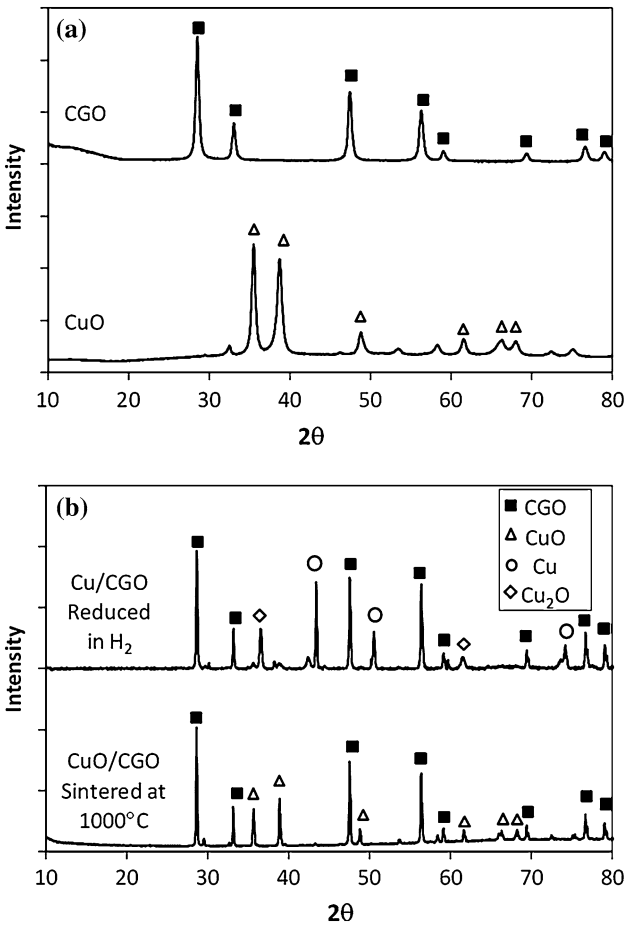

Fig. 5 XRD patterns for **a** the starting material CuO and CGO powder and **b** CuO/CGO electrode after sintering and Cu/CGO electrode after reduction in H_2

resistance and ionic conductivity of the 250-μm-thick YSZ electrolyte at 750 °C were determined experimentally to be 0.96 Ω cm^2 and 0.026 S cm^{-1}, respectively, similar to the estimated value of 0.021 S cm^{-1} using a correlation reported in the literature [29]. The conductivity for a Ni/YSZ electrode was reported as 86 S cm^{-1} at 750 °C, corresponding to an apparent resistance of 4.6×10^{-4} Ω cm^2 for a 40-μm-thick electrode [30]. The discrepancy between the experimental ohmic resistance and the theoretical value could have been due to contact resistance between the current collector and the electrode or from the inaccuracy arising from extrapolating the impedance data to intersect the real axis. In principle, with 50 vol% Ni and Cu contents in the Ni/YSZ and Cu/CGO electrodes, both exceeded the percolation threshold of ca. 40 vol% and the resistance from Ni/YSZ and Cu/CGO electrode should have been negligible compared to that of YSZ electrolyte. However, a Cu/YSZ electrode with 40 vol% Cu and a porosity of 52.2 % was reported [26] as having an apparent conductivity of 0.11 S cm^{-1} at 700 °C, corresponding to a resistance of 0.36 Ω cm^2 for a 40-μm-thick electrode. The

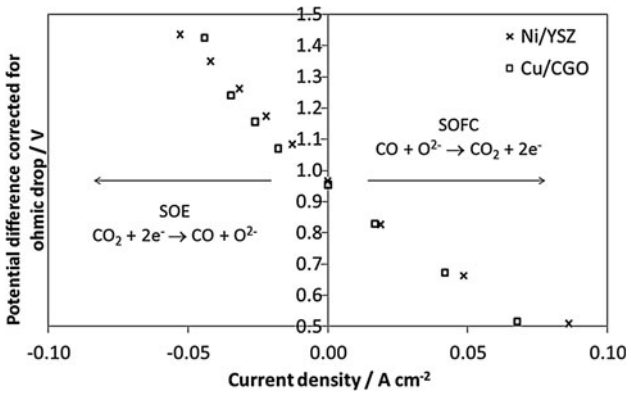

Fig. 6 Potential difference–current density relationship of cells with a Ni/YSZ and a Cu/CGO electrode, operating in both fuel cell mode (SOFC) and electrolysis mode (SOE) with a feed CO_2–CO ratio of 50:50 at 750 °C

Table 1 Area-specific polarisation resistance of the cells with Ni/YSZ and Cu/CGO fuel electrodes estimated from the potential difference–current density data in Fig. 6

Electrode	Area-specific polarisation resistance/Ω cm^2	
	Ni/YSZ	Cu/CGO
SOFC mode	4.68	6.58
SOE mode	8.76	10.1

ohmic resistance of Cu/CGO|YSZ was 40 % higher than that of the Ni/YSZ|YSZ. This could be explained by the difference in thickness of the electrode layers (42 μm for Cu/CGO and 37 μm for Ni/YSZ) and the Ni/YSZ exhibited better microstructure. As shown in Fig. 3, larger pores were present in the Cu/CGO electrode and the distributions of Cu and CGO particles were not as uniform as in the case of the Ni/YSZ electrode, which could lead to a lower connectivity of the Cu particles/network resulting in higher ohmic resistance.

The experimental open circuit potential (OCP) for the Ni/YSZ and Cu/CGO electrodes was 0.963 and 0.954 V, respectively, close to the theoretical OCP value of 0.969 V predicted by the Nernst equation for the same conditions. For both types of fuel electrode, the ohmic drop-corrected potential difference–current density relationships were close to linear in both fuel cell mode and electrolysis mode. The area-specific polarisation resistance (R_p) can be estimated from the gradient of the ohmic drop-corrected potential difference–current density plots, summarised in Table 1. The area-specific polarisation resistance ranged from the lowest value for SOFC mode on Ni/YSZ electrode at 4.68 Ω cm^2 to the highest value for SOE mode on Cu/CGO electrode at 10.1 Ω cm^2, whilst the ohmic resistance for Ni/YSZ|YSZ and Cu/CGO|YSZ electrodes was 1.23 and 1.73 Ω cm^2, respectively, indicating that kinetics and/or mass transfer also played important roles in affecting

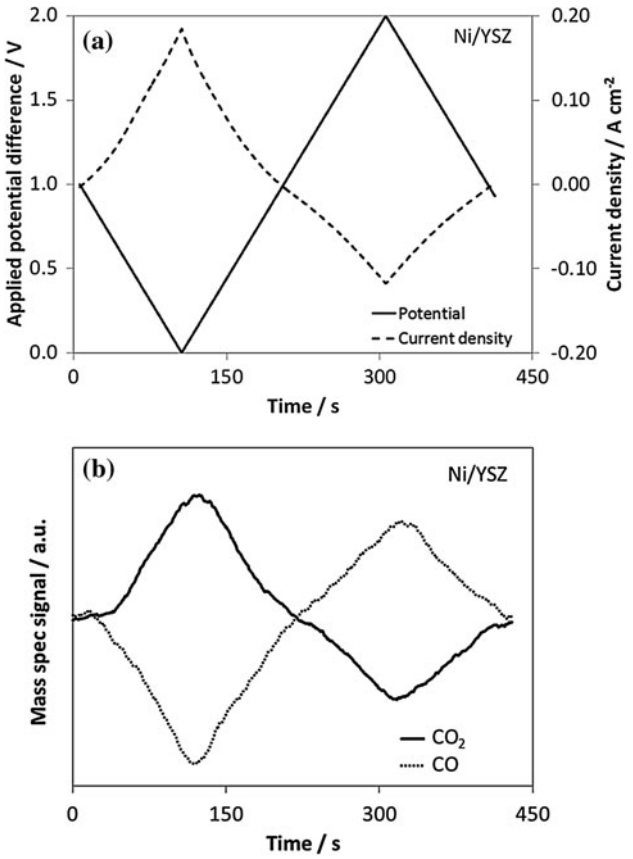

Fig. 7 **a** Cyclic voltammogram and **b** the corresponding CO_2–CO signal for CO_2–CO reactions on the Ni/YSZ electrode, at 750 °C and a CO_2–CO (50:50) feed

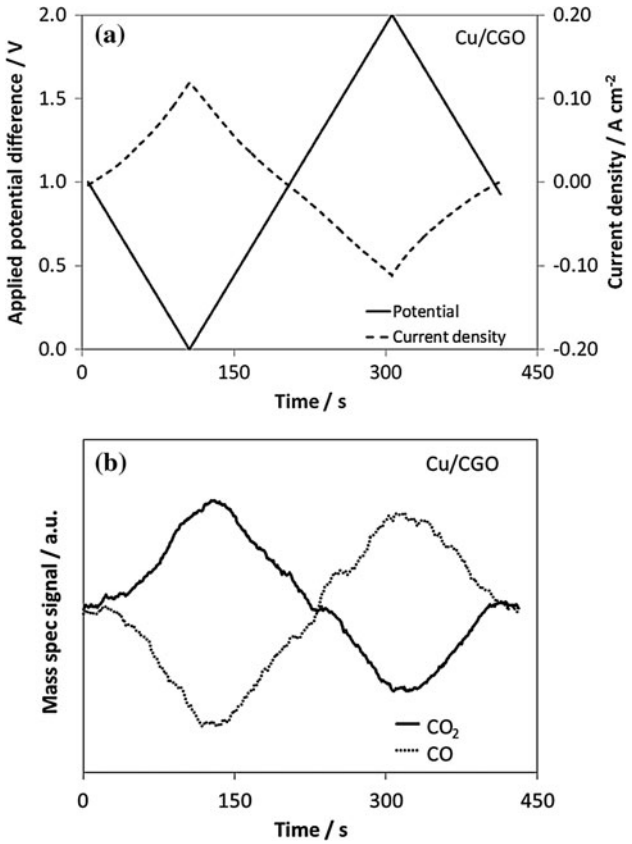

Fig. 8 **a** Cyclic voltammogram and **b** the corresponding CO_2–CO signal for CO_2–CO reactions on the Cu/CGO electrode, at 750 °C and a CO_2–CO (50:50) feed

the cell performance. Though comparable cell performances were achieved, the Ni/YSZ electrode exhibits better performance than the Cu/CGO electrode in both the fuel cell mode for CO oxidation and in the electrolysis mode for CO_2 reduction. However, it cannot be concluded that the catalytic activity of the Cu/CGO electrode was inferior to that of Ni/YSZ electrode for the CO_2–CO reaction, since the SEM images in Fig. 3 showed that the Ni/YSZ electrode probably had a greater TPB density than the Cu/CGO electrode. The reduction of CO_2 was slower than the oxidation of CO on both Ni/YSZ and Cu/CGO electrodes, consistent with observations reported in the literature for Ni/YSZ electrodes [11] and for LSCM/CGO electrodes [14]. This could be explained by the slower diffusion rate of CO_2 molecules than CO molecules through the porous electrodes and/or slower kinetics for CO_2 reduction than CO oxidation.

In order to confirm that the current supplied to the cells was used for CO_2–CO reactions, the composition of the outlet gas from the fuel electrode was determined by a mass spectrometer. Figure 7 shows (a) a cyclic voltammogram and (b) a trace of the CO_2–CO mass spectrometer signal for the cell with a Ni/YSZ electrode, at 750 °C and 50:50 CO_2–CO feed; Fig. 8a, b shows the corresponding data for the Cu/CGO electrode.

For both Ni/YSZ and Cu/CGO electrodes, the fuel electrode applied potential was swept from OCP to 0 to 2 V to OCP at a scan rate of 0.01 V s^{-1}. Between OCP and 0 V, the cell functioned as a SOFC and the oxidation current increased/decreased with overpotential, the current densities peaking at 0 V. As the oxidation current increased and CO was oxidised on the fuel electrode to form CO_2, the CO signal decreased and CO_2 signal increased accordingly. The cell operated as a SOE between OCP and 2 V and CO_2 was reduced on the fuel electrode to form CO by reaction (1). The CO–CO_2 signal followed the trend of the reduction current accordingly and they were mirror images of each other as expected. Signals for H_2 and O_2 were also recorded during the voltammetry and no significant deviation from their baseline values was observed, confirming that any H_2O or O_2 present in the CO_2–CO inlet gas was negligible.

In the SOFC mode, a current density of 0.18 A cm^{-2} was obtained for the Ni/YSZ electrode at 0 V, significantly higher than the 0.12 A cm^{-2} achieved for the Cu/CGO electrode at the same applied potential. This was consistent

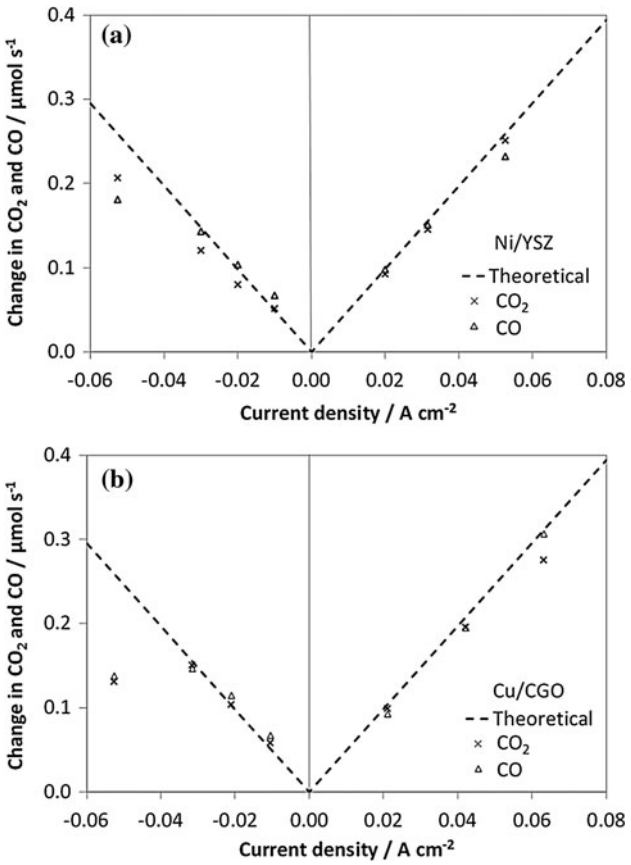

Fig. 9 Current density and the change in CO_2 and CO detected by mass spectrometer, under steady-state operation for **a** Ni/YSZ electrode and **b** Cu/CGO electrode

with the observation from the steady-state potential difference–current density data in Fig. 6. The faster rate of CO oxidation on Ni/YSZ could be due to a greater triple-phase boundary density and faster kinetics on the Ni/YSZ electrode. However, as mentioned earlier, this cannot be confirmed without methods of controlling and quantifying the electrodes' microstructures.

In the SOE mode at an applied potential of 2 V, the current density of Ni/YSZ and Cu/CGO electrodes was −0.12 and −0.11 A cm^{-2}, respectively. The difference in current densities was much smaller than in the case of the SOFC mode.

For the Ni/YSZ electrode, the maximum absolute current density for the oxidation of CO was 50 % higher than that of CO_2 reduction, supported by the amplitudes of the CO_2–CO mass spectrometry signals.

However, the difference in the maximum absolute current density of the SOFC and SOE cycles on the Cu/CGO electrode was less than 10 %, which was much smaller than expected from the steady-state data. The amplitude of the CO_2–CO signal in the SOFC mode was around 25 % higher than that in the SOE cycle, indicating a side reaction. This was likely to be the partial reduction of the CGO component of the Cu/CGO electrode, as explained by Fig. 11 below.

Note that whilst the CO–CO_2 signals obtained from mass spectrometry provided complementary information to the applied potential-current density data, the signals were not quantified and the two sets of signals for the two electrodes should not be compared with each other directly.

To quantify the amount of CO_2–CO reacted/produced by the fuel electrodes, helium was introduced as a carrier gas and the signals were calibrated against controlled CO_2–CO/He flow rates; the feed He–CO_2–CO ratio was 60:20:20 vol%. Figure 9 shows the change in CO_2 and CO in the outlet stream from the fuel electrode detected by mass spectrometry against current density, under steady-state operation for (a) Ni/YSZ electrode and (b) Cu/CGO electrode. Assuming CO oxidation/CO_2 reduction was the only reaction occurring on the fuel electrode in the fuel cell and electrolytic modes, respectively, the theoretical change of CO–CO_2 can be predicted by Faraday's law:

$$I = 2F\frac{\mathrm{d}n}{\mathrm{d}t} \tag{7}$$

I is the current in A, F is the faraday constant (96485 C mol^{-1}) and dn/dt is the change in CO–CO_2 in mol s^{-1}.

For both Ni/YSZ and Cu/CGO electrodes in the fuel cell mode, the change in CO–CO_2 measured experimentally was very close to the theoretical values, confirming that the oxidation of CO was the only reaction that occurred on the fuel electrode. For both Ni/YSZ and Cu/CGO in the electrolytic mode, the change in CO–CO_2 measured experimentally was close to the theoretical values for reduction current densities up to −0.03 A cm^{-2}. At −0.05 A cm^{-2}, the applied potential difference for Ni/YSZ and Cu/CGO electrodes was 2 and 2.1 V, respectively; the change in CO and CO_2 measured experimentally was smaller than theoretical values, indicating that reaction(s) besides CO_2 reduction to CO occurred. The change in CO_2 concentration was similar to that for CO, taking into account accuracy limitation of the measurements, suggesting that the side reaction did not involve CO_2–CO. A current efficiency of only 24.7 % has been reported [17] for CO_2 electrolysis using a SOE with a lanthanum strontium titanate (LST)/CGO fuel electrode, YSZ electrolyte and LSM/CGO air electrode, at a cell potential difference of 2 V. The reasons for the loss of current efficiency observed only in the SOE mode, but not in the SOFC mode at similar absolute values of overpotentials, will be explained below.

The applied potential was increased further to 2.5 V to determine the onset potential of electronic conduction of the YSZ electrolyte for the SOE. Figure 10 shows the applied potential (E_{app}), fuel electrode potential against ring reference electrode, against current density of cells

with (a) Ni/YSZ and (b) Cu/CGO electrode, with a feed CO_2–CO ratio of 50:50 at 750 °C. The fuel electrode applied potential was swept from OCP to 2.5 V at a rate of 0.01 V s^{-1}, causing current densities to increase almost linearly up to ca. 2 V, followed by exponential increase in current density for both cells. This behaviour was observed for all cells tested, regardless of the type of fuel electrode or metal content (data not shown here). Applied potentials of >2.5 V caused irreversible damage to the cells. Mass spectrometry data showed that the amount of CO_2 reduced did not follow the exponential increase in current. The additional reduction current at greater potentials was due to the reduction of, e.g. Zr^{4+} to Zr^{3+} in the YSZ electrolyte. Also, a rise in cell temperature was measured for applied potentials >2 V as some of the electrical current supplied was converted to heat. This type of applied potential–current density relationship and the electronic conduction of YSZ electrolyte have also been reported for H_2O electrolysis in SOEs with YSZ electrolytes [31]. The decomposition potential for YSZ (10 mol% yttria) with an air reference electrode at 900 °C was reported as 2.23 V and the corresponding equilibrium oxygen partial pressure as 9.6×10^{-40} atm [32].

Figure 11 shows the experimental data of oxygen partial pressure (P_{O_2}) and decomposition potential (E_{dp}) for YSZ (10 mol% yttria) with an air | LSM reference electrode [32]. A linear relationship can be determined from the data in [32] for the effect of temperature on the decomposition potential (E_{dp}), Eq. (8), and the corresponding oxygen partial pressure (P_{O_2}), Eq. (9). A decomposition potential of 2.30 V and oxygen partial pressure of 5.26×10^{-45} atm at 750 °C were predicted by extrapolation. This explained the irreversible damage to the cell caused by applying potentials up to 2.5 V, exceeding the decomposition potential of YSZ.

$$E_{dp} = 2.847 - 5.3 \times 10^{-4} T \quad (8)$$

$$\log(P_{O_2}) = 0.0357 \times T - 80.8 \quad (9)$$

The temperature-dependent equilibrium potential $\Delta E^{\theta}_{ZrO_2/Zr,T}$ for the decomposition of ZrO_2 by reaction may be calculated by Eq. (10) using thermodynamic data from [33].

$$ZrO_2 \rightarrow Zr + O_2 \quad (10)$$

$$\Delta E^{\theta}_{ZrO_2/Zr,T} = -\Delta_r G^{\theta}_T/(4F) \quad (11)$$

The resulting data plotted in Fig. 11 predict a value of 2.35 V at 750 °C, similar to the experimental value of 2.30 V for YSZ (10 mol% yttria) electrolyte. Similarly, the temperature-dependent equilibrium potential $\Delta E^{\theta}_{CeO_2/Ce_2O_3,T}$ for the reduction of CeO_2 to Ce_2O_3 by reaction (12) may be calculated by Eq. (13) using thermodynamic data from [33–36] as also shown in Fig. 11.

$$4CeO_2 \rightleftarrows 2Ce_2O_3 + O_2 \quad (12)$$

$$\Delta E^{\theta}_{CeO_2/Ce_2O_3,T} = -\Delta_r G^{\theta}_T/(4F) \quad (13)$$

The ionic conductivity (σ_{ion}) of YSZ (8 mol% yttria) was 0.021 S cm^{-1} at 750 °C, predicted by the empirical correlation in Eq. (14) [29]. Increasing applied potential caused a decrease in equilibrium oxygen pressure at the CO_2–CO electrode, propagating through the YSZ electrolyte and resulting in an increase in electronic conduction of YSZ. The electronic conductivity (σ_e) of YSZ at various potentials and oxygen pressure, predicted by the empirical correlation, Eq. (15), [29] is summarised in Table 2. The equilibrium oxygen pressure P_{O_2} at potential E and temperature T was estimated by Eq. (16) [32]. k is the Boltzmann's constant, $(8.614 \times 10^{-5}$

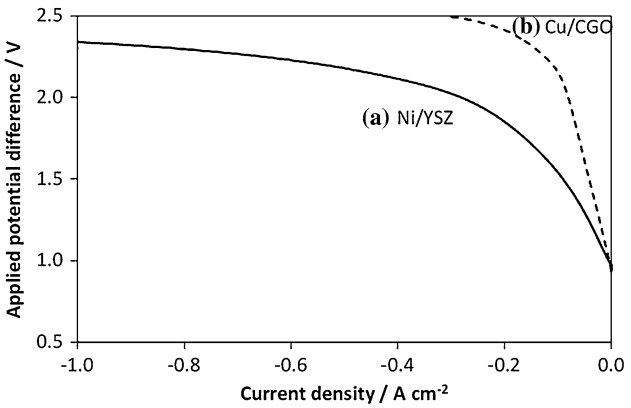

Fig. 10 Applied potential difference–current density relationship of cells with *a* Ni/YSZ and *b* Cu/CGO electrode, with a feed CO_2–CO ratio of 50:50 at 750 °C, applied potential swept from OCP to 2.5 V at a rate of 0.01 V s^{-1}

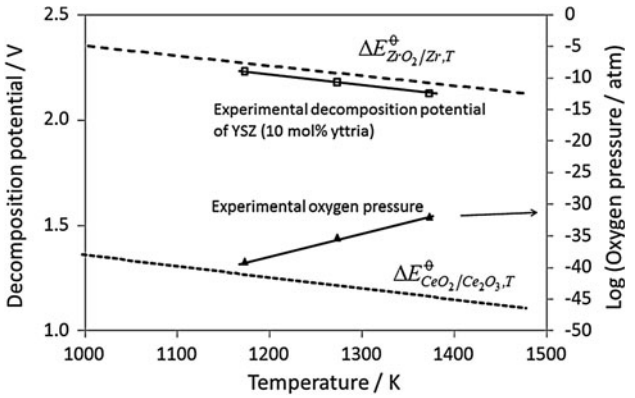

Fig. 11 Effects of temperature on the theoretical decomposition potential of ZrO_2 [33], the equilibrium potential of the reduction of CeO_2 to Ce_2O_3 [33–36], experimental data of decomposition potential (E_{dp}) for YSZ (10 mol% yttria) with an air reference electrode and the corresponding oxygen partial pressure (P_{O_2}) [32]

eV K^{-1}), and $P^{R}_{O_2}$ is the oxygen pressure at the reference electrode ($P^{R}_{O_2} = 0.21$ atm for an air reference electrode).

$$\sigma_{ion} = 1.63 \times 10^2 \exp\left(\frac{-0.79\text{eV}}{kT}\right) \quad (14)$$

$$\sigma_e = 1.31 \times 10^7 \exp\left(\frac{-3.88\text{eV}}{kT}\right) P_{O_2}^{-1/4} \quad (15)$$

$$E = \frac{kT}{4e} \ln\left(\frac{P^{R}_{O_2}}{P_{O_2}}\right) \quad (16)$$

For potentials <1.5 V, the electronic conductivity (σ_e) of YSZ was insignificant compared to its ionic conductivity (σ_{ion}). A majority of SOEs for CO_2/H_2O electrolysis reported in the literature were operated within this potential range. At 1.8 and 2.0 V, σ_e was 5 and 50 % of σ_{ion}, respectively. As potentials increased beyond 1.8 V, a decrease in current efficiencies was expected and determined experimentally. At 2.2 V, σ_e was 4.8 times greater than σ_{ion} and most of the current would short circuit through the electrolyte as electronic current. As a result of this property, under galvanostatic operation in the SOE mode, even if the CO_2 feed was interrupted, the cell potential would be limited due to this non-destructive electronic conduction of YSZ, which could prevent the potential from reaching that required for destructive electrolyte reduction. Similar effects have been reported for SOEs used for steam electrolysis with YSZ electrolytes [31]. SOEs should be operating at potentials (<1.5 V) far from those at which electronic conduction or decomposition of YSZ electrolytes occurred, as higher potentials lead to low current and thermodynamic efficiencies and large electrical energy consumptions.

As mentioned earlier, the loss of current efficiency caused by increasing electronic conduction of YSZ at greater overpotentials was observed only in the SOE mode and not in the SOFC mode. In the former case, at large cathode overpotentials, reduction of CO_2 on Ni/YSZ or Cu/CGO cathode via reaction (1) ($CO_2 + 2e^- \rightarrow CO + O^{2-}$) could occur in parallel with electrolyte decomposition reactions such as (10) or (12). Such conditions would be exacerbated when the intrinsic rate of CO_2 reduction became faster than CO_2 mass transport rates to the cathode's surface, causing CO_2 starvation and hence partial electronic conduction of YSZ. In the fuel cell mode, the potentials required for reductive decomposition of electrolytes are not accessible.

As shown by equilibrium potential predicted for the reduction of CeO_2 to Ce_2O_3 in Fig. 11, together with the results mentioned previously from Fig. 8, the CGO in Cu/CGO electrode was also expected to be partially reduced for the applied potentials used in the SOE mode.

Table 2 Electronic conductivity predictions for YSZ at 750°C

Potential/V	Equilibrium P_{O_2}/atm	Electronic conductivity, σ_e/S cm^{-1}
1.3	4.95×10^{-27}	3.7×10^{-6}
1.5	5.65×10^{-31}	3.6×10^{-5}
1.8	6.89×10^{-37}	0.0011
2.0	7.86×10^{-41}	0.0105
2.2	8.96×10^{-45}	0.1016

3.3 Effect of CO_2–CO feed ratio on Cu/CGO electrode

For the electrolysis of CO_2 by reaction (17),

$$CO_2 \rightarrow CO + 0.5O_2 \quad (17)$$

the temperature-dependent standard equilibrium potential may be calculated from Eq. (18):

$$\Delta E^{\theta}_{CO_2/CO,T} = -\Delta_r G^{\theta}_T/(2F) \quad (18)$$

using thermodynamic data obtained from [37], giving Eq. (19):

$$\Delta E^{\theta}_{CO_2/CO,T} = 4.52 \times 10^{-4} T - 1.466 \quad (19)$$

The Nernst equation at temperature T, taking into account the composition of reactants and products, $\Delta E(T)$, i.e. the equilibrium or theoretical open circuit potential (OCP), is expressed by Eq. (20):

$$E(T) = \Delta E^{\theta}_{CO_2/CO,T} + \frac{RT}{2F} \ln\left(\frac{P_{CO_2}}{P_{CO}\sqrt{P_{O_2}}}\right) \quad (20)$$

Therefore, for any CO_2/CO pressure ratio, the equilibrium potential ($\Delta E(T)$ *or* OCP) is a linear function of temperature, as shown in Fig. 12. (P_{O_2}= 0.21 atm as the air electrode was exposed to ambient air.)

The theoretical and experimental open circuit potentials (OCP) for different CO_2–CO feed ratios at 750 °C are summarised in Table 3. Experimental OCPs increased from 0.820 to 1.035 V as the CO_2–CO ratio decreased from

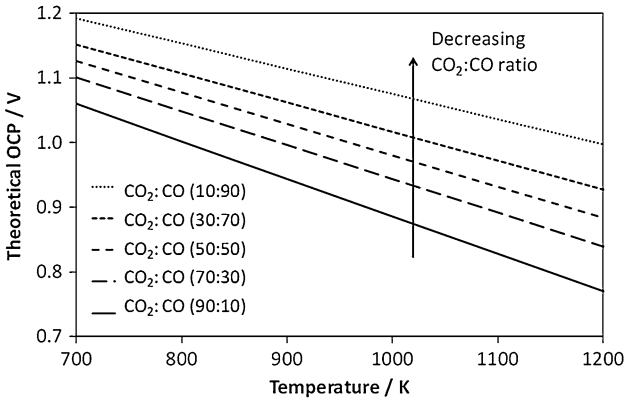

Fig. 12 Effects of temperature on theoretical OCP for different CO_2–CO feed ratios

Table 3 Theoretical and experimental open circuit potentials (OCP) for different CO_2–CO feed ratios at 750 °C

CO_2/CO ratio	Theoretical OCP/V	Experimental OCP/V
90:10	0.872	0.820
70:30	0.932	0.919
50:50	0.969	0.954
30:70	1.007	0.985
10:90	1.066	1.035

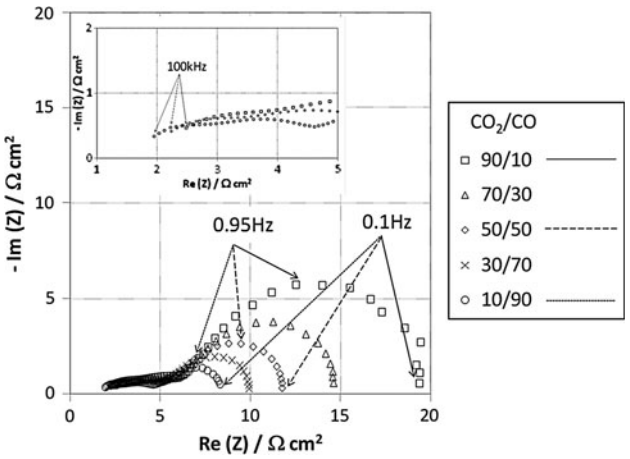

Fig. 13 Impedance spectra of the Cu/CGO fuel electrode operating at 750 °C at OCP with different CO_2–CO feed ratios

Table 4 Summary of resistance obtained from the impedance spectra data in Fig. 13

CO_2–CO	R_s/Ωcm^2	R_p/Ωcm^2
90:10	2.00	17.96
70:30	1.81	13.23
50:50	1.72	10.36
30:70	1.67	8.50
10:90	1.43	7.36

90:10 to 10:90 and were similar to the theoretical values predicted by the Nernst equation (20).

Figure 13 shows impedance spectra of the Cu/CGO fuel electrode operating at 750 °C at OCP with different CO_2–CO feed ratios. The ohmic and polarisation resistances obtained from Fig. 13 are summarised in Table 4. The high frequency intercept with the real axis (R_s) represents the total ohmic resistance of the YSZ electrolyte, the Cu/CGO electrode and contact resistance (s). As the experimental data did not intersect the real axis directly, R_s was determined using commercial impedance fitting software (Nova 1.6, Metrohm Autolab). The ohmic resistance, R_s, decreased by 28.5 % as the CO_2–CO ratio was

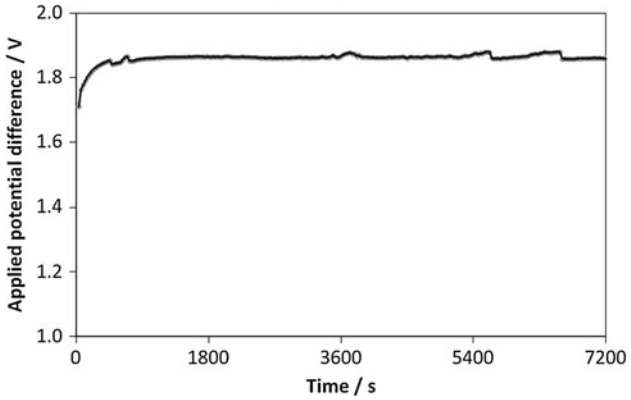

Fig. 14 Potential difference against time at a controlled current density of −0.01 A cm^{-2} for a Cu/CGO electrode, at 750 °C and a feed CO_2–CO ratio of 70:30

decreased from 90:10 to 10:90. At 750 °C and in reducing atmospheres, CeO_2 was partially reduced from Ce^{4+} to Ce^{3+}, generating electronic charge carriers by reaction (21), causing CGO to behave as a mixed ionic–electronic conductor [38]. This occurred with decreasing CO_2–CO ratio, resulting in increased electronic conductivity in CGO and hence decrease in R_s.

$$O_O = V_{\ddot{O}} + 2e^- + 0.5O_2 \quad (21)$$

O_O represents oxygen at a regular oxygen site and $V_{\ddot{O}}$ is a vacant positively charged oxygen site.

The polarisation resistance (R_p) was the sum of the resistances from the high frequency arc and the low frequency arc. The high frequency arcs were highly depressed semi-circles due to the porous nature of the electrodes, whilst the low frequency arcs were less depressed. As the CO_2–CO ratio was decreased from 90:10 to 10:90, the oxygen pressure (P_{O_2}) decreased and R_p decreased by 60 % from 17.96 to 7.36 Ω cm^{-2}.

A similar small semi-circular high frequency arc to that shown in Fig. 13 has been reported for a LSCM/CGO electrode [15] at 750 °C under OCP in a CO_2–CO (70:30) atmosphere. As the temperature was increased to 900 °C, it developed into a Gerischer-like impedance dispersion with linear response (45° to real axis) at high frequency.

Significant decrease in resistance from the low frequency arc for a LSCM/CGO electrode was measured with decreasing CO_2–CO ratio [14], ascribed to dissociative adsorption and surface diffusion of the active species on the electrode surface. Similar effects on the low frequency arc resistance have also been reported using a CGO (40 mol% gadolinium) electrode [13], for which the decrease was explained by increasing kinetically active utilisation thickness, surface exchange rate and vacancy diffusion coefficient of CGO with decreasing P_{O_2}.

3.4 Short-term stability

Figure 14 shows the time dependence of reactor potential difference at a current density of -0.01 A cm^{-2} for a Cu/CGO electrode at 750 °C and a feed of CO_2–CO ratio of 70:30. Potential differences increased from 1.7 to 1.85 V in the first 10 min, then stabilised over the remaining 2 h of the experiment, suggesting that the kinetics of any degradation processes were sufficiently slow not to affect such short-term performances. The Cu/CGO electrode was stable at 1.85 V in the CO_2–CO atmosphere at 750 °C without significant Cu sintering/migration, carbon deposition or electrode delamination. The next step is to optimise the Cu content and microstructure of the Cu/CGO electrode and investigate its long-term stability.

4 Conclusions

The feasibility was investigated of using a Cu/CGO electrode for CO_2 reduction to CO in a high temperature solid oxide electrolyser (CO_2–CO, Cu/CGO|YSZ|YSZ/LSM|LSM, ambient air). An adherent layer of porous Cu/CGO electrode on YSZ electrolyte was achieved by sintering Cu/CGO paste at 1,000 °C for 5 h. The cell was operated in both fuel cell and electrolyser modes. Comparable performances were obtained with Ni/YSZ and Cu/CGO fuel electrodes for CO_2 electrolysis at 750 °C and a 50:50 CO_2–CO feed. Oxidation rates of CO were faster than reduction rates of CO_2 on both types of fuel electrodes. Ohmic and polarisation resistances of the Cu/CGO electrode all decreased with decreasing CO_2–CO feed ratio. In the electrolytic mode with the Cu/CGO electrode, 100 % current efficiency for CO_2 reduction to CO was achieved up to 1.5 V. As reactor potential differences were increased, the YSZ electrolyte became increasingly electronically conductive, causing a loss in current efficiency. Further increase in potential difference to ca. >2.3 V caused irreversible damage to the YSZ electrolyte due to its decomposition. During 2 h of operation of the Cu/CGO electrode at 1.85 V and 750 °C for CO_2 electrolysis, no significant performance degradation, Cu sintering/migration, carbon deposition or electrode delamination was evident. Further work includes (a) improving Cu/CGO electrode performance by optimisation of its Cu content and microstructure, (b) investigating the long-term stability of the optimised electrode and (c) improving electrode stability against high temperature by addition of cobalt (Co) or formation of Cu/Ni alloys.

Acknowledgments The authors thank the UK Engineering and Physical Sciences Research Council for funding a post-doctoral research associateship for C-y.C. and a doctoral training studentship for LK.

References

1. Jensen SH, Larsen PH, Mogensen M (2007) Hydrogen and synthetic fuel production from renewable energy sources. Int J Hydrogen Energy 32:3253–3257
2. Sridhar KR, Vaniman BT (1997) Oxygen production on Mars using solid oxide electrolysis. Solid State Ion 93:321–328
3. Tao G, Sridhar KR, Chan CL (2004) Study of carbon dioxide electrolysis at electrode/electrolyte interface: part I. Pt/YSZ interface. Solid State Ion 175:615–619
4. Tao G, Sridhar KR, Chan CL (2004) Study of carbon dioxide electrolysis at electrode/electrolyte interface: part II. Pt-YSZ cermet/YSZ interface. Solid State Ion 175:621–624
5. Ebbesen SD, Mogensen M (2009) Electrolysis of carbon dioxide in solid oxide electrolysis cells. J Power Sour 193:349–358
6. Graves C, Ebbesen SD, Mogensen M (2011) Co-electrolysis of CO_2 and H_2O in solid oxide cells: performance and durability. Solid State Ion 192:398–403
7. Graves C, Ebbesen SD, Mogensen M, Lackner KS (2011) Sustainable hydrocarbon fuels by recycling CO_2 and H_2O with renewable or nuclear energy. Renew Sustain Energy Rev 15:1–23
8. Zhan Z, Zhao L (2010) Electrochemical reduction of CO_2 in solid oxide electrolysis cells. J Power Sources 195:7250–7254
9. Stoots C, O'Brien J, Hartvigsen J (2009) Results of recent high temperature coelectrolysis studies at the Idaho National Laboratory. Int J Hydrogen Energy 34:4208–4215
10. Zhan Z, Kobsiriphat W, Wilson JR, Pillai M, Kim I, Barnet SA (2009) Syngas production by co-electrolysis of CO_2/H_2O: the basis for a renewable energy cycle. Energy Fuels 23:3089–3096
11. Kim-Lohsoontorn P, Laosiripojana N, Bae J (2011) Performance of solid oxide electrolysis cell having bi-layered electrolyte during steam electrolysis and carbon dioxide electrolysis. Curr Appl Phys 11:S223–S228
12. Kim-Lohsoontorn P, Bae J (2011) Electrochemical performance of solid oxide electrolysis cell electrodes under high-temperature coelectrolysis of steam and carbon dioxide. J Power Sources 196:7161–7168
13. Green RD, Liu CC, Adler SB (2008) Carbon dioxide reduction on gadolinia-doped ceria cathodes. Solid States Ion 179:647–660
14. Yue X, Irvine JTS (2012) Alternative cathode material for CO_2 reduction by high temperature solid oxide electrolysis cells. J Electrochem Soc 159(8):F442–F448
15. Yue X, Irvine JTS (2012) Impedance studies on LSCM/GDC cathode for high temperature CO_2 electrolysis. Electrochem Solid State Lett 15(3):B31–B34
16. Bidrawn F, Kim G, Corre G, Irvine JTS, Vohs JM, Gorte RJ (2008) Efficient reduction of CO_2 in a solid oxide electrolyzer. Electrochem Solid State Lett 11(9):B167–B170
17. Li S, Li Y, Gan Y, Xie K, Meng G (2012) Electrolysis of H_2O and CO_2 in an oxygen-ion conducting solid oxide electrolyzer with a $La_{0.2}Sr_{0.8}TiO_{3-\delta}$ composite cathode. J Power Sources 218:244–249
18. Huang TJ, Chou CL (2009) Electrochemical CO_2 reduction with power generation in SOFCs with Cu-added LSCF–GDC cathode. Electrochem Commun 11:1464–1467
19. Gattrell M, Gupta N, Co A (2006) A review of the aqueous electrochemical reduction of CO_2 to hydrocarbons at copper. J Electroanal Chem 594:1–19
20. Huang TJ, Shen XD, Chou CL (2009) Characterization of Cu, Ag and Pt added $La_{0.6}Sr_{0.4}Co_{0.2}Fe_{0.8}O_{3-\delta}$ and gadolinia-doped ceria as solid oxide fuel cell electrodes by temperature-programmed techniques. J Power Sources 187:348–355
21. Gorte RJ, Vohs JM (2011) Catalysis in solid oxide fuel cells. Annu Rev Chem Biomol Eng 2:9–30

22. Jacobson AJ (2010) Materials for solid oxide fuel cells. Chem Mater 22:660–674
23. Mclntosh S, Gorte RJ (2004) Direct hydrocarbon solid oxide fuel cells. Chem Rev 104:4845–4865
24. Kiratzis N, Holtappels P, Hatchwell CE, Mogensen M, Irvine JTS (2001) Preparation and characterization of copper/yttria titania zirconia cermets for use as possible solid oxide fuel cell anodes. Fuel cells 1:211–218
25. Lee S, Kang KH, Kim JM, Hong HS, Yun Y, Woo SK (2008) Fabrication and characterization of Cu/YSZ cermet high-temperature electrolysis cathode material prepared by high-energy ball-milling method I. 900°C-sintered. J Alloys Compd 448:363–367
26. Lee S, Kim JM, Hong HS, Woo SK (2009) Fabrication and characterization of Cu/YSZ cermet high temperature electrolysis cathode material prepared by high-energy ball-milling method II. 700°C-sintered. J Alloys Compd 467:614–621
27. Kim J, Lee S, Kang KH, Hong HS (2010) Preparation and characterization of Cu/YSZ cathode for high-temperature electrolysis. Int J Energy Res 34:438–444
28. Ruiz-Morales JC, Canales-Vazquez J, Marrero-Lopez D, Pena-Martınez J, Tarancon A, Irvine JTS, Nunez P (2008) Is YSZ stable in the presence of Cu? J Mater Chem 18:5072–5077
29. Park JH, Blumenthal RN (1989) Electronic transport in 8 mole percent Y_2O_3–ZrO_2. J Electrochem Soc 136:2867–2876
30. Li PW, Chyu MK (2003) Simulation of the chemical/electrochemical reactions and heat/mass transfer for a tubular SOFC in a stack. J Power Sources 124:487–498
31. Schefold J, Brisse A, Zahid M (2009) Electronic conduction of yttria-stabilized zirconia electrolyte in solid oxide cells operated in high temperature water electrolysis. J Electrochem Soc 156(8): B897–B904
32. Weppner W (1977) Formation of intermetallic Pt–Zr compounds between Pt electrodes and ZrO_2-based electrolytes, and the decomposition voltage of yttria-doped ZrO_2. J Electroanal Chem 84:339–350
33. Chase MW (1998) NIST-JANAF thermochemical tables. In: Linstrom PJ, Mallard WG (eds) NIST chemistry webbook, NIST Standard Reference Database Number 69. National Institute of Standards and Technology, Gaithersburg, p 20899. http://webbook.nist.gov. Accessed 17 Jan 2013
34. Carl YL (2009) Yaws' handbook of thermodynamic properties for hydrocarbons and chemicals. Knovel, New York. http://www.knovel.com/web/portal/browse/display?_EXT_KNOVEL_DISPLAY_bookid=2380&VerticalID=0. Accessed 22 Jan 2013
35. King EG, Christensen AU (1961) High-temperature heat contents and entropies of cerium dioxide and columbium dioxide. U.S. Dept. of the Interior, Bureau of Mines, Washington
36. Huntelaar ME, Booij AS, Cordfunke EHP, van der Laan RR, van Genderen ACG, van Miltenburg JC (2000) The thermodynamic properties of $Ce_2O_{3(s)}$ from T → 0 K to 1500 K. J Chem Thermodyn 32:465–482
37. Gurvich LV, Iorish VS, Yungman VS, Dorofeeva OV (2006) Thermodynamic properties as a function of temperature. In: Lide DR (ed) CRC Handbook of Chemistry and Physics, 87th edn. CRC Press, Boca Raton, 5:43-5:65
38. Liu J, Weppner W (1999) Electronic conductivity measurement of gadolinia doped ceria by DC-partial-polarization. Ionics 5:115–121